Structural OFF/ON transitions of myosin in relaxed porcine myocardium predict calcium activated force

Weikang Ma[1], Timothy S. McMillen[2], Matthew Carter Childers[2], Henry Gong[1], Michael Regnier[2], Thomas Irving[1]

1. Biology, Illinois Institute of Technology, Chicago, IL, USA,
2. Bioengineering, University of Washington, Seattle, WA, USA

Supplemental Material

Methods

X-ray Diffraction

Frozen porcine left ventricle wall was prepared as described previously (1). Briefly, the frozen muscle was thawed in skinning solution (91 mM K^+-propionate, 3.5 mM MgCl, 0.16 mM $CaCl_2$, 7 mM EGTA, 2.5 mM Na_2ATP, 15 mM creatine phosphate, 20 mM Imidazole, 30 mM BDM, 1% Triton-X100 and 3% dextran at pH 7) at room temperature before dissection into smaller strips. These myocardium strips were skinned at room temperature for 3 hours. Samples were then washed with relaxing solution (91 mM K^+-propionate, 3.5 mM MgCl, 0.16 mM $CaCl_2$, 7 mM EGTA, 2.5 mM Na_2ATP, 15 mM creatine phosphate, 20 mM Imidazole and 3% dextran at pH 7) for three times, 10 min each. Well-aligned fiber bundles were further dissected into preparations with a length of 4 mm with a diameter of 200 µm prior to attachment of aluminum T-clips to both ends.

X-ray diffraction experiments were performed at the BioCAT beamline 18ID at the Advanced Photon Source, Argonne National Laboratory (2). The X-ray beam energy was set to 12 keV (0.1033 nm wavelength) at an incident flux of ~5×10^{12} photons per second. The specimen to detector distance was about 2.5 m. One end of the preparation was then attached to a hook on a force transducer (Model 402B Aurora Scientific Inc., Aurora, ON, Canada) and the other end

to a static hook. The muscle was incubated in a customized chamber with Kapton™ windows and mounted in the X-ray path. The bottom of chamber was attached to a heat exchanger, so the solution was maintained between 28 °C to 30 °C. The chamber was connected to a multiway valve syringe pump (Hamilton model 500) for remote solution changes. The muscle fiber bundles were stretched to a sarcomere length of 2.3 µm using micromanipulators attached to the hooks while monitoring light diffraction patterns from a helium-neon laser (633 nm). X-ray diffraction patterns were collected on a MarCCD 165 detector (Rayonix Inc., Evanston IL) with a 1 s exposure time as a function of five increasing dATP compositions (0%, 2%, 10%, 25%, and 100%) with the total NTP concentration (dATP + ATP) remaining constant at 2.5 mM after 10 min incubation in each solution.

To minimize radiation damage, the muscle was oscillated along its horizontal axes at a velocity of 2 mm/s. The radiated areas were moved vertically after each exposure to avoid overlapping X-ray exposures. Two to three patterns were collected under each condition and the X-ray reflection spacing and intensity data extracted from these patterns were averaged.

X-ray data analysis

The data were analyzed using data reduction programs belonging to the open-source MuscleX software package developed at BioCAT (3). The equatorial reflections were measured by the “Equator” routine in MuscleX as described previously (4). X-ray patterns were averaged together with the “Quadrant Folding” routine in MuscleX to improve the signal-to-noise ratio and the diffuse scattering from disordered components in the sarcomere was subtracted from the X-ray diffraction patterns prior to analysis. The intensities and spacings of meridional and layer line reflections were measured by the “Projection Traces” routine in MuscleX as described previously (5, 6). R_m was estimated as previously described (7). Briefly, the distance from the first maximum of MLL1 in the intensity distribution to the meridian in the reciprocal lattice (r) is inversely related to the radius to the center of mass of the cross-bridges (R_m) based on a J3 Bessel function with

the argument $4.2 = 2 \times \pi \times r \times R_m$. To compare the intensities under different conditions, the measured intensities of X-ray reflections were normalized to the intensities of the sixth-order actin-based layer line which do not change under relaxed conditions (see figure 3D)

Mechanical experiments

Frozen ventricular wall tissue was thawed and de-membranated in relaxing solution (in mM: 100 KCl, 10 imidazole, 2 EGTA, 5 MgCl2, and 4 ATP) containing 50% glycerol (vol:vol) and 1% Triton X-100 overnight at 4°C then stored in glycerinated relaxing solution without triton at −20°C and used within one week. De-membranating and storage solutions contained protease inhibitor cocktail (P8340; Sigma-Aldrich). Thin left ventricular strips (118±23 μm wide and 0.822±0.18mm long) were dissected out of the endocardium with cells aligned in a single direction. Ends of the strips were wrapped in aluminum T-clips and mounted between a motor (Aurora Scientific, Model 312B) and force transducer (Aurora Scientific, Model 403A). Sarcomere length (SL) was set to 2.3 μm by stretching the sample to ~15% over non-strained length. Steady-state force was measured using a custom-built mechanical apparatus at 28°C during Ca^{2+} activation at various concentrations in presence of 2.5 mM ATP or dATP with half of the preparations measured first in ATP and half in dATP. Experimental solutions were maintained pH 7.0 at 28°C and contained (in mM): 15 phosphocreatine, 15 EGTA, 80 MOPS, 1 free Mg2+, 1 DTT, and 5 Mg2ATP or 5 Mg2dATP and 3g/100mL dextran. Ca^{2+} concentration (reported as $pCa = -\log[Ca^{2+}]$) was adjusted by varying amounts of $CaCl_2$. Ionic strength was set to 0.17 M with KCl. Relaxing and activating solutions were prepared using a custom software package as described previously (8). Passive force (pCa 8.0) was subtracted from force at other pCa concentrations to calculate Ca activated force. For additional demonstration of the ability of dATP to increase contraction, force was measured at submaximal (pCa=5.7) and maximal (pCa=4.0) Ca^{2+} activation first in ATP, then dATP and back to ATP. The average value of both ATP activations was used to eliminate the

effect of activation order. Stiffness was determined by small amplitude (0.05% Ls) sinusoidal length oscillations (1 kHz), as reported previously (9).

Molecular modeling

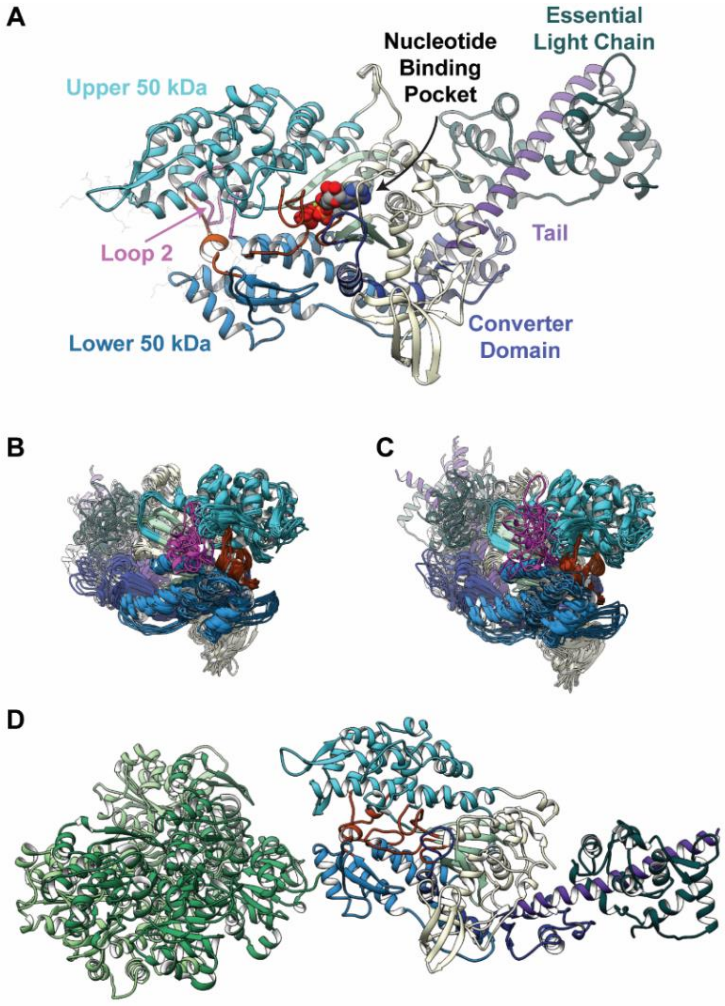

Figure S1. Molecular Models used in DelPhiForce Electrostatics Calculations. (A) The starting conformation of bovine b-cardiac myosin + ADP.Pi + essential light chain is colored to highlight functional regions. The myosin motor is comprised of four domains: the N-terminal domain (pale yellow), upper and lower 50 kDa domains (cyan, blue), and converter domain (dark blue) organized around the nucleotide binding pocket. The tail (purple) is connected to the converter domain via a flexible hinge and contains IQ sequence motifs that interact with the essential light chain (dark green). The actin binding cleft is formed between the upper and lower 50 kDa domains and includes loop 2 (magenta). (B) The 10 myosin+ADP.Pi and (C) 10 myosin+dADP.Pi structures used in DelPhiForce calculations have been aligned on residues in

the upper 50 kDa domain. Comparison of the aligned structures highlights the increased conformational variability in loop 2 and the lower 50 kDa domain when dADP is bound in the nucleotide binding pocket. (D) Example actin (green) and myosin protein complex used for input to DelPhiForce after a 20 Å shift of myosin away from its binding site on actin.

Molecular model building. Starting coordinates for bovine (*Bos taurus*) cardiac-myosin II motor domain (residues 4-810) and essential light chain (residues 39-199) in the pre-powerstroke (Myosin + ADP.Pi + Mg^{2+}) state were obtained from an X-ray crystal structure in the Protein Data Bank (PDB, www.rcsb.org (10)) solved by Houdusse et al (PDB ID: 5N69, 2.45 Å resolution) (11) Chains A (myosin motor domain) and H (essential light chain) were chosen for simulation, atoms from OM were removed, and the vanadate ion (VO_4) was replaced with an inorganic phosphate ion (P_i). Then, missing heavy atoms were built using *Modeller* (12). These starting coordinates were used to generate an additional system in which ADP was replaced by 2'-deoxy-ADP (dADP) via removal of the 2' oxygen (Figure S1A). These systems will be referred to as myosin+ADP.P_i and myosin+dADP.P_i, respectively. Next, hydrogen atoms were modeled onto the structures using the *leap* module of *AMBER* and each protein was solvated with explicit water molecules in a periodic, truncated octahedral box that extended 10 Å beyond any protein atom. Finally, Na^+ and Cl^- counterions were added to neutralize the systems.

Force Field and Molecular Mechanics. All simulations were performed with the *AMBER* package (13) and the ff14SB force field (14). Water molecules were treated with the TIP3P force field (15). Metal ions were modeled using the Li and Merz parameter set (16, 17). ADP, dADP, and P_i molecules were treated with the GAFF2 force field (18) with custom parameters derived from QM simulations using *ORCA* (19). The SHAKE algorithm was used to constrain the motion of hydrogen-containing bonds (20, 21). Long-range electrostatic interactions were calculated using the particle mesh Ewald (PME) method.

Pre-production protocols. Each system was minimized in three stages in the presence of atomic restraints: first, hydrogen atoms were minimized; second, all solvent atoms were minimized; third,

all atoms were minimized. After minimization, systems were heated to 310 K over 300 ps using the canonical NVT (constant **n**umber of particles, **v**olume, and **t**emperature) ensemble in the presence of atomic restraints. After the system temperatures reached 310 K, the systems were equilibrated over 5 successive stages using the isobaric-isothermal NPT (constant **n**umber of particles, **p**ressure, and **t**emperature) ensemble. During the first 4 stages, the systems were equilibrated for 0.4 ns in the presence of restraints on backbone atoms. The strength of the restraints was decreased from 25 kcal mol^{-1} during the first stage to 1 kcal mol^{-1} during the fourth stage. During the final equilibration stage, the systems were equilibrated for 5 ns in the absence of restraints.

Production MD protocol. Production dynamics for conventional molecular dynamics (MD) simulations were then performed using GPU-accelerated *pmemd.cuda* in the canonical NVT ensemble using an 8 Å nonbonded cutoff, a 2 fs time step, and coordinates were saved every picosecond. Simulations were run in triplicate for 500 ns each (3 microseconds net sampling described here).

MD Analysis. Trajectories were analyzed every 10 picoseconds. The solvent accessible surface area (SASA) was calculated using the *surf* command of *cpptraj*. The surface area was calculated for three separate regions: the actin binding interface (400-411, 364-369, 636-642, 529-545, and 569-576), loop 2 (residues 620-643), and the actin binding interface excluding loop 2 residues. Residues that form the actin binding interface were inferred from a cryo-electron microscopy structure of bovine myosin in complex with chicken skeletal actin and human cardiac tropomyosin in the rigor state (PDB ID: 6X5Z) (22). Molecular graphics were rendered with *UCSF Chimera* and *VMD*.

Selection of Structures for Electrostatics Calculations. The MD trajectories were filtered according to the SASA of residues within loop 2 and the actin binding interface. We extracted all trajectory frames for which the surface area of these regions was within 50 $Å^2$ of the ensemble averages of the myosin+ADP.P_i and myosin+dADP.P_i simulations. The filtered trajectories were

then clustered on the Ca atoms of residues in loop 2 and the actin binding interface. Representative snapshots of the top 10 most populous clusters in each of the filtered myosin+ADP.P_i (Fig S1B) and myosin+dADP.P_i (Fig S1C) trajectories were selected for electrostatics calculations.

Electrostatics Calculations. We used *DelPhi* and *DelPhiForce* to analyze electrostatic interactions between pre-powerstroke myosin and actin, to analyze how those electrostatic interactions were modulated by the replacement of ADP with dADP, and to analyze how separation of actin and myosin affected electrostatic interactions. Initial coordinates for DelPhi calculations were prepared as follows. First, an actin tetramer (containing two monomers from each actin protofilament) was generated from the 6X5Z structure. This tetramer was positioned against a bound myosin in 6X5Z, then the tropomyosins, other actins, and other myosins were removed from 6X5Z. Then, the 20 MD-derived myosin/ELC snapshots were structurally aligned to the 6X5Z myosin using *UCSF Chimera* (23). Backbone heavy atoms in the upper 50 kDa domain were used to perform the alignment. This resulted in the placement of our 20 filtered structures in an approximate actin-bound orientation; however, because our simulations were performed using pre-powerstroke myosin, the actin binding cleft did not have the correct geometry to allow for true actin-myosin interactions. Next, we defined a plane passing through those heavy atoms that formed interactions between the actin tetramer and 6X5Z myosin (actin:myosin interactions were defined using default settings in the *Find Clashes/Contacts* dialog of *UCSF Chimera*). Next, the remaining 6X5Z myosin was removed and the MD-derived myosin snapshots were shifted away from the actin tetramer along a vector normal to the previously defined plane. Actin tetramer and myosin coordinates were saved after shifting the myosins 20 Å away (Fig S1D) and again after the myosins were shifted a total of 30 Å away. Nonstandard ligand atoms (ADP, dADP, P_i, Mg^{2+}) were removed prior to electrostatics calculations. We used *pdb2pqr* (24) to

generate PQR files from the actin and myosin coordinates. Then, the *DelPhiForce* (25, 26) script was used to evaluate electrostatic interactions between actin and myosin. The default parameters were chosen with the exception of the salt concentration, which was set to 170 mM to best match our experimental results. *DelPhiForce* results were visualized with *VMD*. We analyzed the net electrostatic force exerted on myosin by actin, the projection of this force along the normal vector used to shift myosin atoms away from actin, as well as the force acting on individual myosin residues. Data were analyzed using custom *Python* scripts employing the *NumPy, SciPy*, and *Matplotlib Python* libraries (27-29).

Statistics

Statistical analyses were performed using GraphPad Prism 9 (Graphpad Software). The results are given as mean ± SEM. One-way repeated measures ANOVA with the Geisser-Greenhouse correction and Tukey's multiple comparisons test with individual variances computed for each comparison was performed for the data shown in Figure 2 and in Figure 3 except for figure 2B where the data was analyzed by fitting a mixed model with the Geisser-Greenhouse correction and mixed-effects analysis was performed for multiple comparisons tests. The increases in $I_{1,1}/I_{1,0}$, S_{M6}, relative force at pCa4 and pCa 5.7 in figure 5 were fit with one phase association functions (Y = Y0 + (Plateau –Y0)(1-exp(-Kx)), where half-value is computed as ln(2)/K) and the relative decreases of √IMLL1, and √IM3 in figure 5 were fit with one phase exponential decays (Y = (Y0 - Plateau)(exp(-Kx)) + Plateau), where half-value is computed as ln(2)/K). Student's two-tailed t-test with equal variance was performed on data presented in figure 5A-D, figure 6 and figure 7. Symbols on figures: ns: p>=0.05, *: p<0.05, **: p<0.01, ***: p<0.001 and ****: p<0.0001.

Table S1. Changes in X-ray reflection parameters in response to increased dATP concentrations.

Parameter	Meaning	0% dATP	2% dATP	10% dATP	25% dATP	100% dATP	100% /0 %
$I_{1,1}/I_{1,0}$	Proximity of myosin heads to actin	0.38±0.01	0.43±0.015	0.51±0.025	0.62±0.037	0.70±0.05	1.84
R_m (nm)	Radius of myosin heads from center of thick filament	14.06±0.13	14.73±0.13	14.07±0.16	14.12±0.1	13.98±0.04	0.99
I_{MLL1} (a.u.)	Helical ordering of the myosin heads	1.58±0.06	1.36±0.11	0.99±0.12	0.65±0.10	0.63±0.08	0.40
I_{M3} (a.u.)	Axial ordering of the myosin heads	1.09±0.05	0.97±0.06	0.68±0.08	0.47±0.05	0.42±0.05	0.39
S_{M6} (nm)	Thick filament backbone periodicity	7.186±0.004	7.194±0.004	7.205±0.005	7.214±0.004	7.213±0.003	1.0038
I_{ALL6} (a.u.)	Intensity of reflection from the left-handed actin helix in the thin filament	1.31±0.07	1.25±0.05	1.3±0.05	1.28±0.05	1.27±0.05	0.97

Table S2. Calcium activated contractile properties of porcine myocardium at different dATP concentrations.

pCa	8	6	5.8	5.6	5.4	5.2	5	4
Tension in ATP, (mN/mm^2)	0	3.5 ± 0.7	25.4±2.1	62.5±6.7	75.0±7.5	79.2±8.4	80.8±9.0	81.7±12.8
Tension in dATP, (mN/mm^2)	5.2 ± 1.6	11.5 ± 1.1	44.3±4.5	75.3±11.1	85.5±11.1	87.8±10.8	88.2±10.8	90.8±15.8
dATP %	0	2	10	25	50			
Relative force at pCa 5.7	1.0	0.98±0.04	1.21±0.04	1.51±0.09	1.50±0.05			
Relative force at pCa 4	1.0	0.99±0.01	1.04±0.005	1.08±0.014	1.15±0.03			

Table S3. Stiffness (in MPa) at different pCa from pCa 8 to pCa 4 at ATP (n = 12) and different dATP (n = 6) concentrations.

pCa	ATP	2% dATP	10% dATP	25% dATP	100% dATP
8	0.62±0.02	0.81±0.10	0.76±0.05	0.95±0.09	0.95±0.12
6	0.89±0.03	0.95±0.11	0.93±0.04	1.15±0.11	1.31±0.14
5.8	2.03±0.06	2.09±0.25	1.81±0.06	2.18±0.16	3.03±0.30
5.6	4.03±0.10	4.00±0.43	3.88±0.14	4.04±0.16	4.64±0.45
5.4	4.72±0.10	4.62±0.44	4.59±0.14	4.66±0.15	5.02±0.48
5.2	5.02±0.11	4.96±0.46	4.86±0.14	5.02±0.17	5.26±0.48
5	5.17±0.11	5.10±0.48	5.05±0.15	5.07±0.15	5.28±0.49
4	5.22±0.12	5.31±0.51	5.35±0.19	5.29±0.19	5.44±0.51

Table S4 Statistical comparisons between conditions.

Conditions	*p* (2A)	*p* (2B)	*p* (3A)	*p* (3B)	*p* (3C)	*p* (4C)	*p* (4D)
0 % vs. 2%	0.0089	0.0028	0.3308	0.3575	0.0234	0.9963	0.4737
0 % vs. 10 %	0.0027	>0.9999	0.0029	0.0055	<0.0001	0.0002	0.0084
0 % vs. 25 %	0.0004	0.9821	<0.0001	<0.0001	0.0002	<0.0001	0.0196
0 % vs. 100 %	0.0006	0.9065	<0.0001	<0.0001	<0.0001	<0.0001	0.0206
2 % vs. 10 %	0.0286	0.019	0.0122	0.006	0.0025	0.0043	0.0562
2 % vs. 25 %	0.0006	0.2257	0.0003	0.0002	0.001	<0.0001	0.016
2 % vs. 100 %	0.0005	0.0303	0.0003	<0.0001	0.0017	<0.0001	0.0232
10 % vs. 25 %	0.0108	0.9995	0.1635	0.2591	0.1195	<0.0001	0.2659
10 % vs. 100 %	0.0116	0.9641	0.1385	0.0883	0.3581	0.0001	0.081
25 % vs. 100 %	0.0391	0.7821	0.9982	0.8171	0.9902	0.9995	0.4413

References

1. W. Ma *et al.*, Myofibril orientation as a metric for characterizing heart disease. *Biophysical journal* **121**, 565-574 (2022).
2. R. Fischetti *et al.*, The BioCAT undulator beamline 18ID: a facility for biological non-crystalline diffraction and X-ray absorption spectroscopy at the Advanced Photon Source. *J. Synchrotron Radiat.* **11,**, 399-405 (2004).
3. J. Jiratrakanvong *et al.*, MuscleX: software suite for diffraction X-ray imaging V1.13.1. doi:10.5281/zenodo.1195050. doi:10.5281/zenodo.1195050 (2018).
4. W. Ma, H. Gong, T. Irving, Myosin Head Configurations in Resting and Contracting Murine Skeletal Muscle. *Int J Mol Sci* **19** (2018).
5. W. Ma *et al.*, Thick-Filament Extensibility in Intact Skeletal Muscle. *Biophysical journal* **115**, 1580-1588 (2018).
6. B. Kiss *et al.*, Nebulin stiffens the thin filament and augments cross-bridge interaction in skeletal muscle. *Proceedings of the National Academy of Sciences of the United States of America* **115**, 10369-10374 (2018).
7. W. Ma *et al.*, The Super-Relaxed State and Length Dependent Activation in Porcine Myocardium. *Circulation research* **129**, 617-630 (2021).
8. D. A. Martyn *et al.*, Unloaded shortening of skinned muscle fibers from rabbit activated with and without Ca2+. *Biophysical journal* **67**, 1984-1993 (1994).
9. M. Regnier *et al.*, Cross-bridge versus thin filament contributions to the level and rate of force development in cardiac muscle. *Biophysical journal* **87**, 1815-1824 (2004).
10. H. M. Berman *et al.*, The Protein Data Bank. *Nucleic Acids Res* **28**, 235-242 (2000).
11. V. J. Planelles-Herrero, J. J. Hartman, J. Robert-Paganin, F. I. Malik, A. Houdusse, Mechanistic and structural basis for activation of cardiac myosin force production by omecamtiv mecarbil. *Nat Commun* **8**, 190 (2017).
12. N. Eswar *et al.*, Comparative protein structure modeling using Modeller. *Curr Protoc Bioinformatics* **Chapter 5**, Unit-5 6 (2006).
13. D. A. Case, H. M. Aktulga, K. Belfon, S. R. B. I.Y. Ben-Shalom, D.S. Cerutti, T.E. Cheatham, III, G.A. Cisneros, V.W.D. Cruzeiro, T.A. Darden, R.E. Duke, G. Giambasu, M.K. Gilson, H. Gohlke, A.W. Goetz, R. Harris, S. Izadi, S.A. Izmailov, C. Jin, K. Kasavajhala, M.C. Kaymak, E. King, A. Kovalenko, T. Kurtzman, T.S. Lee, S. LeGrand, P. Li, C. Lin, J. Liu, T. Luchko, R. Luo, M. Machado, V. Man, M. Manathunga, K.M. Merz, Y. Miao, O. Mikhailovskii, G. Monard, H. Nguyen, K.A. O'Hearn, A. Onufriev, F. Pan, S. Pantano, R. Qi, A. Rahnamoun, D.R. Roe, A. Roitberg, C. Sagui, S. Schott-Verdugo, J. Shen, C.L. Simmerling, N.R. Skrynnikov, J. Smith, J. Swails, R.C. Walker, J. Wang, H. Wei, R.M. Wolf, X. Wu, Y. Xue, D.M. York, S. Zhao, and P.A. Kollman (2021) Amber. (University of California, San Francisco.).
14. J. A. Maier *et al.*, ff14SB: Improving the Accuracy of Protein Side Chain and Backbone Parameters from ff99SB. *J Chem Theory Comput* **11**, 3696-3713 (2015).
15. W. L. Jorgensen, J. Chandrasekhar, J.D. Madura, R.W. Impey, and M.L. Klein., Comparison of simple potential functions for simulating liquid water. *The Journal of chemical physics* **79**, 926–935. (1983).
16. P. Li, K. M. Merz, Jr., Taking into Account the Ion-induced Dipole Interaction in the Nonbonded Model of Ions. *J Chem Theory Comput* **10**, 289-297 (2014).
17. P. Li, L. F. Song, K. M. Merz, Jr., Parameterization of highly charged metal ions using the 12-6-4 LJ-type nonbonded model in explicit water. *The journal of physical chemistry. B* **119**, 883-895 (2015).

18. J. Wang, R. M. Wolf, J. W. Caldwell, P. A. Kollman, D. A. Case, Development and testing of a general amber force field. *J Comput Chem* **25**, 1157-1174 (2004).
19. F. Neese, The ORCA program system. *WIREs Computational Molecular Science* **2**, 73-78 (2012).
20. K. D. Hammonds, D. M. Heyes, Shadow Hamiltonian in classical NVE molecular dynamics simulations involving Coulomb interactions. *The Journal of chemical physics* **154**, 174102 (2021).
21. S. Miyamoto, P. A. Kollman, Settle: An analytical version of the SHAKE and RATTLE algorithm for rigid water models. *Journal of Computational Chemistry* **13**, 952-962 (1992).
22. M. H. Doran *et al.*, Cryo-EM and Molecular Docking Shows Myosin Loop 4 Contacts Actin and Tropomyosin on Thin Filaments. *Biophysical journal* **119**, 821-830 (2020).
23. E. F. Pettersen *et al.*, UCSF Chimera--a visualization system for exploratory research and analysis. *J Comput Chem* **25**, 1605-1612 (2004).
24. H. Kather, B. Simon, Antagonistic effects of prostaglandin E1 and nicotinic acid on the human fat cell adenylate cyclase. *Res Commun Chem Pathol Pharmacol* **23**, 81-88 (1979).
25. L. Li, A. Chakravorty, E. Alexov, DelPhiForce, a tool for electrostatic force calculations: Applications to macromolecular binding. *J Comput Chem* **38**, 584-593 (2017).
26. L. Li *et al.*, DelPhi: a comprehensive suite for DelPhi software and associated resources. *BMC Biophys* **5**, 9 (2012).
27. C. R. Harris *et al.*, Array programming with NumPy. *Nature* **585**, 357-362 (2020).
28. P. Virtanen *et al.*, SciPy 1.0: fundamental algorithms for scientific computing in Python. *Nature methods* **17**, 261-272 (2020).
29. J. D. Hunter, Matplotlib: A 2D Graphics Environment. *Computing in Science & Engineering* **9**, 90-95 (2007).